

Mid-infrared intersubband absorption in strain-balanced non-polar (In)AlGa_N/InGa_N multi-quantum wells

TRANG NGUYEN,¹ BRANDON DZUBA,^{1,2} YANG CAO,¹ ALEXANDER SENICHEV,^{1,2} ROSA E. DIAZ,² MICHAEL J. MANFRA,^{1,2,3,4} AND OANA MALIS^{1,*} 

¹Department of Physics and Astronomy, Purdue University, West Lafayette, Indiana 47907, USA

²Birck Nanotechnology Center, Purdue University, West Lafayette, Indiana 47907, USA

³School of Electrical and Computer Engineering, Purdue University, West Lafayette, Indiana 47907, USA

⁴School of Material Engineering, Purdue University, West Lafayette, Indiana 47907, USA

*omalis@purdue.edu

Abstract: Mid-infrared intersubband transitions in strain-balanced m-plane (In)Al_xGa_{1-x}N/In_{0.16}Ga_{0.84}N (0.19 ≤ x ≤ 0.3) multi-quantum wells are reported for the first time in the range of 3.4–5.1 μm (244–360 meV). Direct and attenuated total-reflection infrared absorption measurements are interpreted using structural information revealed by high-resolution x-ray diffraction and transmission electron microanalysis. The experimental intersubband energies are better reproduced by calculations using the local-density approximation than the Hartree-Fock approximation for the exchange-correlation correction. The effect of charge density, quantum well width, and barrier alloy composition on the intersubband transition energy is also investigated to evaluate the potential of this material for practical device applications.

© 2021 Optical Society of America under the terms of the [OSA Open Access Publishing Agreement](#)

1. Introduction

III-nitride semiconductors including AlN, GaN, InN and their alloys have been successfully used in ultraviolet and visible optoelectronic devices with tremendous impact on society [1–6]. Moreover, they have recently gained attention as promising materials for intersubband (ISB) devices in the infrared (IR) range of the spectrum (1.5–60 μm) [7–14]. The substantial and widely tunable conduction band offset (CBO) coupled with a large longitudinal-optical phonon energy (92 meV) and sub-picosecond ISB relaxation times [7,13] of nitride materials make them ideal for use in IR devices. Most research on nitride intersubband transitions over the past decade has focused on c-plane heterostructures [15–17]. However, because of the asymmetric quantum wells (QWs) that result from strong built-in polarization fields along the c-axis [18], these materials are challenging for use in practical nitride IR optoelectronics. Fortunately, the symmetry of the wurtzite crystal allows nitride heterostructures to be grown along the nonpolar (10–10) direction - also called the m-plane direction - that eliminates built-in polarization fields completely.

Intersubband absorption (ISBA) experiments in nonpolar nitrides first focused on m-plane AlGa_N/Ga_N multi-quantum wells (MQWs) [14,19,20]. We reported far- and mid-IR ISBA on m-plane AlGa_N/Ga_N MQWs grown by plasma-assisted molecular beam epitaxy (MBE) [9,21,22]. Most recently, Monavarian et al. measured ISB transitions with record narrow linewidth in m-plane AlGa_N/Ga_N grown with ammonia MBE [23]. However, the AlGa_N/Ga_N system is not scalable to thick devices due to the significant lattice-mismatch between the component materials. Moreover, an unexpected challenge arose with growth of high Al mole fraction m-plane AlGa_N [10,24,25]. We found that plasma-assisted MBE growth of AlGa_N on m-plane Ga_N exhibits an instability that prevents growth of planar, homogeneous AlGa_N alloys above 60% Al-composition [9,10]. To overcome these obstacles, we investigate m-plane (In)AlGa_N/InGa_N MQWs that

are nearly strain-balanced to GaN. This material combination minimizes strain accumulation in the epilayer relative to the GaN substrate by compensating the tensile strain of AlGa_N barriers with compressive strain of InGa_N wells in each MQW period. Therefore, relatively thick ISB structures can be grown while simultaneously avoiding the AlGa_N growth instability by keeping the Al mole fraction below 30%. These m-plane AlGa_N/InGa_N heterostructures also provide CBOs that can theoretically support ISB transitions in the technologically relevant near-IR range.

Nonpolar m-plane AlGa_N/InGa_N heterostructures exhibit their own set of specific material growth challenges [26,27] that, so far, limited research on their infrared properties. Pesach et al. were the first to report ISB absorption in m-plane AlGa_N/InGa_N [11], but no significant experimental work has been published since. Building on our recent progress on MBE growth of m-plane InGa_N [27], we performed a systematic in-depth study of the influence of structural parameters on ISBA energy in m-plane (In)_xAl_{1-x}Ga_{1-x}N/In_yGa_{1-y}N MQWs ($x = 0.16 - 0.3$, $y = 0.16$) grown by plasma-assisted MBE. This paper specifically scrutinizes the effects of quantum well width, barrier Al composition, and doping level on mid-IR ISB transition energies of non-polar AlGa_N/InGa_N MQWs. The experimental results are compared with calculations of ISB transition energies including many-body corrections. The local density approximation (LDA) is found to better predict the m-plane nitride ISBA energies than the Hartree-Fock approximation (HFA) likely due to better estimation of correlation effects. The ultimate goal is to evaluate the potential of m-plane (In)AlGa_N/InGa_N heterostructures for near-IR devices.

2. Experimental and calculation details

All samples discussed in this study consist of multiple InGa_N quantum wells with AlGa_N barriers grown on m-plane (10–10)-oriented free-standing GaN substrates by plasma-assisted molecular beam epitaxy. The substrates were purchased from Nanowin Science and Technologies and have a threading dislocation density less than $5 \times 10^6 \text{ cm}^{-2}$, a root mean squared (RMS) roughness less than 0.3 nm over a $4 \times 4 \mu\text{m}^2$ area, and a miscut of $-0.5^\circ \pm 0.2^\circ$ towards the (0001) direction. The substrates were first sonicated in trichloroethylene, acetone, and methanol, rinsed with deionized water, and dried with N₂ gas. Due to the relatively small size of the substrates (5 mm × 10 mm), they were gallium-mounted on 2-inch GaN on sapphire wafers and outgassed overnight (> 12 hours) in an ultra-high vacuum chamber before being loaded in the MBE chamber. The MBE machine is equipped with standard effusion cells for gallium, indium, aluminum, and silicon, while nitrogen is supplied by a Veeco Unibulb radio frequency (RF) plasma source operating at 300 W power with 0.5 sccm N₂ flow rate. These conditions correspond to a nitrogen limited GaN growth rate of $\sim 7.9 \text{ nm/min}$, or $\sim 5.8 \times 10^{14} \text{ atoms/cm}^2\text{s}$ nitrogen flux. An $\sim 150 \text{ nm}$ GaN buffer layer was grown under gallium rich conditions at 720°C prior to growth of the active layers.

The structural details of the select group of samples discussed in detail in this paper are summarized in Table 1. All layers were grown with an indium surfactant at 565°C. More details about the growth procedure are given in [28]. We have previously shown that these conditions enable the growth of coherently strained, homogeneous In_{0.16}Ga_{0.84}N layers up to 30 nm thick [27], and AlGa_N/InGa_N MQW structures with improved barrier material homogeneity, reduced surface roughness, and decreased interface roughness [28]. The indium surfactant present during barrier growth resulted in unintentional incorporation of a small amount of indium in the AlGa_N barriers and, henceforth, the barrier material is referred to as (In)AlGa_N [28]. The barrier thicknesses of the MQW structures were chosen to minimize strain accumulation. We used the thickness-weighted method to approximate strain-balanced conditions: $\varepsilon_b t_b + \varepsilon_w t_w = 0$ where ε_b and ε_w represent the strain in the barrier and well, respectively, while t_b and t_w represent their respective layer thicknesses. Note that strain is anisotropic on the m-plane surface, and thus cannot be exactly balanced along both the a-axis and c-axis simultaneously. Therefore, to partially mitigate strain, a barrier thickness was chosen in-between the values required to balance strain on each axis independently. Charge was provided to the samples via two silicon δ -doping

sheets in each quantum barrier (QB) located 1 nm away from each interface. The charge density was varied by changing the duration of the silicon δ -doping deposition.

Table 1. Summary of structural parameters, experimental results including ISB absorption energy peaks and full-width-at-half maximum (FWHM) of absorption peaks, and theoretical calculations of the transition energies for a series of m-plane (In)AlGaIn/InGaIn MQWs.

Sample (Group)	QB/QW thickness (nm)	QB/QW alloy composition	Calc. sheet charge density $\times 10^{12} \text{ cm}^{-2}$ / δ -doping duration (s)	Experimental ISBA Energy Peak/FWHM (meV)		Calculated ISBA Energy (meV)	
				ATR	Direct	HFA	LDA
A (I)	7.5/2.8	$\text{Al}_{0.19}\text{In}_{0.06}\text{Ga}_{0.75}\text{N} / \text{In}_{0.16}\text{Ga}_{0.84}\text{N}$	5.37/10	246/65	254/77	342	285
B (I)	5.2/3.16	$\text{Al}_{0.3}\text{Ga}_{0.7}\text{N} / \text{In}_{0.16}\text{Ga}_{0.84}\text{N}$	5.73/10	303/86	329/89	364	293
C (I,II)	5.8/2.9	$\text{Al}_{0.24}\text{In}_{0.02}\text{Ga}_{0.74}\text{N} / \text{In}_{0.16}\text{Ga}_{0.84}\text{N}$	7.39/10	293/71	320/86	357	291
D (II)	5.8/2.9	$\text{Al}_{0.24}\text{In}_{0.02}\text{Ga}_{0.74}\text{N} / \text{In}_{0.16}\text{Ga}_{0.84}\text{N}$	8.01/20	284/124	340/104	359	291
E (II)	6/2.9	$\text{Al}_{0.24}\text{In}_{0.01}\text{Ga}_{0.75}\text{N} / \text{In}_{0.16}\text{Ga}_{0.84}\text{N}$	2.31/2	292/85	308/104	320	281
F (II,III)	6/2.9	$\text{Al}_{0.24}\text{In}_{0.02}\text{Ga}_{0.74}\text{N} / \text{In}_{0.16}\text{Ga}_{0.84}\text{N}$	5.62/5	288/85	303/55	348	290
G (III)	6/2.4	$\text{Al}_{0.24}\text{In}_{0.02}\text{Ga}_{0.74}\text{N} / \text{In}_{0.16}\text{Ga}_{0.84}\text{N}$	5.62/5	323/89	334/91	382	323
H (III)	6/2.1	$\text{Al}_{0.24}\text{In}_{0.03}\text{Ga}_{0.73}\text{N} / \text{In}_{0.16}\text{Ga}_{0.84}\text{N}$	5.52/5	336/218	360/324	394	337
I (III)	9/3.5	$\text{Al}_{0.24}\text{In}_{0.01}\text{Ga}_{0.75}\text{N} / \text{In}_{0.16}\text{Ga}_{0.84}\text{N}$	5.51/5	244/67	257/60	303	245

High-resolution x-ray diffraction (HRXRD) measurements of all structures were conducted using a Panalytical MRD X'Pert Pro high-resolution x-ray diffractometer. To extract structural parameters, modeling of the HRXRD ω - 2θ scans was done using the software package Epitaxy

4.5a provided by Malvern PANalytical. HRXRD does not allow independent determination of individual layer thicknesses and compositions in MQW structures. Therefore, the composition and growth rate of InGaN quantum wells were assumed to be equal to those of similarly grown bulk layers [28]. In addition to this, we assumed that all provided Al is incorporated, and then used this information in the modelling to estimate the thickness and composition of the barrier material.

Structural data from HRXRD was confirmed with high-resolution high-angle annular dark field scanning transmission electron microscopy (HRHAADF-STEM) as shown for representative samples in Fig. 1. The microscopy specimens were prepared using the *in situ* lift-out technique with a Thermo Scientific Helios G4 UX Dual Beam focused ion beam (FIB). The FIB allows samples to be cut with a low energy Ga ion beam in order to minimize ion-induced damage. The specimens were then cleaned with Fischione Nanomill Model 1040 at 900 eV and 120 nA with $\pm 10^\circ$ tilt. Finally, before imaging we used a Fischione Ar Plasma Cleaner to reduce possible contamination from FIB and air. HRHAADF-STEM images were taken with an aberration-corrected Thermo Scientific Themis Z microscope using a voltage of 300 kV, current of 0.24 nA, and 0.65 probe size. This microscope allows the images to be corrected up to the 3rd order of aberration including astigmatism, spherical, coma, etc. Energy-dispersive x-ray spectroscopy (EDS) was performed to collect 2D elemental maps of the active region as well as to confirm the alloy composition extracted by HRXRD. However, due to the large error bar for Al, Ga, and In compositions, EDS results were only used for qualitative information. HRHAADF-STEM imaging indicates sharp interfaces but also identifies regions of higher Al-composition in the barriers. Based on electron microscopy and HRXRD data, we estimate the uncertainty in determining the QW width as ± 0.25 nm and the uncertainty for the Al molar fraction in the barrier as $\pm 1\%$.

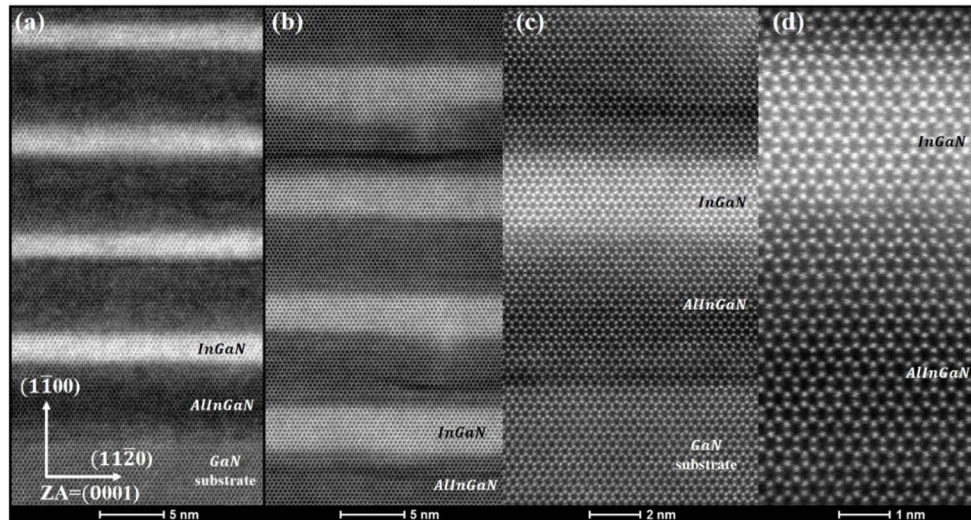


Fig. 1. HRHAADF-STEM of samples H (a) and B (b-d).

The samples were optically characterized with continuous excitation photoluminescence (PL) measurements. For PL experiments, the samples were placed in a liquid He flow cryostat and measured in reflection geometry in the range from 80 K to room temperature. Excitation power of about 10 mW (estimated cw photo-excited carrier density is $6.3 \times 10^{11} \text{ cm}^{-3}$) was provided by a 325 nm cw He-Cd laser. The PL spectra were recorded with a Cary Eclipse fluorescence spectrometer equipped with a photomultiplier tube. We have previously demonstrated that the

use of an indium surfactant during growth of the m-plane AlGaIn barriers of InGaIn MQWs leads to stronger PL intensity and reduced linewidth [28]. Figure 2 shows the low temperature PL for a group of samples discussed in this paper. The PL linewidth is sensitive to small unintentional differences in QW thickness (see samples A and C). These differences arise from uncontrollable growth parameter fluctuations and also lead to differences in interface roughness that are hard to quantify with structural characterization techniques. We also observe a rapid broadening of the PL spectra with increasing doping that we attribute to increased interface roughness and impurity scattering.

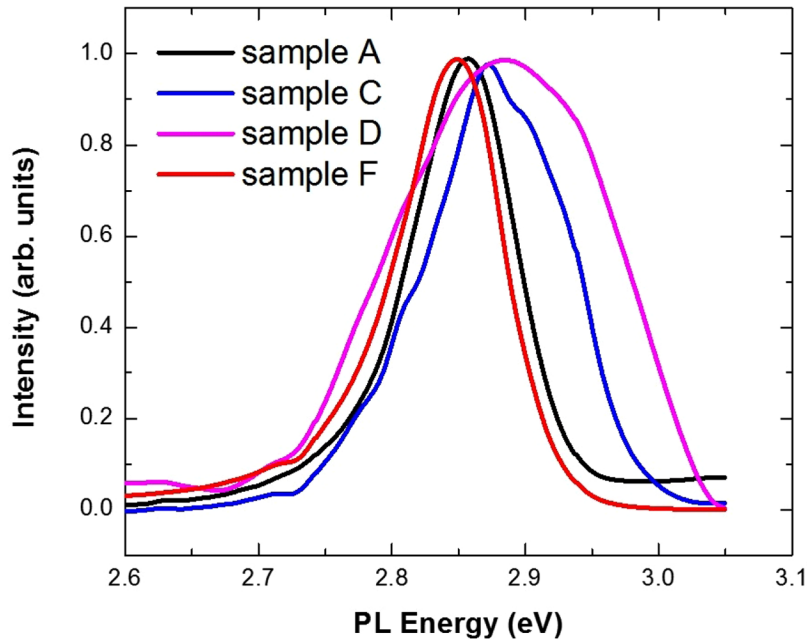


Fig. 2. Photoluminescence (PL) measurements of several structures at liquid nitrogen temperature (80 K). All PL curves were scaled to reach a maximum of 1 arbitrary unit. The linewidths of the spectra are 91 meV, 110 meV, 170 meV, and 96 meV for samples A, C, D, and F, respectively.

A combination of direct Fourier transform infrared (FTIR) spectroscopy and attenuated total reflectance FTIR (ATR-FTIR) is used to perform ISBA measurements on all samples using a Thermo Scientific Nicolet 8700 spectrometer (Fig. 3(a-b)). For direct FTIR measurements, sample preparation involved cleaving samples to small pieces and polishing 45° facets on both sides. In some cases (e.g. sample A), a gold film was deposited on top of the active region to enhance ISBA intensity [29]. For the ATR-FTIR method, the samples were sandwiched with a polished Ge crystal to allow an evanescent wave to probe absorption in the MQW stack [19,20]. This technique is ideal for measuring ISBA in the range where the substrate is opaque. However, as the specimen is squeezed against the Ge crystal, an unintentional air gap between the interfaces may affect the penetration depth of the evanescent wave, and hence, the absorption intensity. Therefore, quantitative results by this technique are sometimes affected by experimental artifacts. The ISBA spectra were obtained by first normalizing the p- and s-polarized transmission spectra to the backgrounds, and then taking the ratio of the p- to the s-polarized spectra [21,30]. For the ATR-FTIR, the backgrounds were collected in transmission through the Ge crystal without any sample.

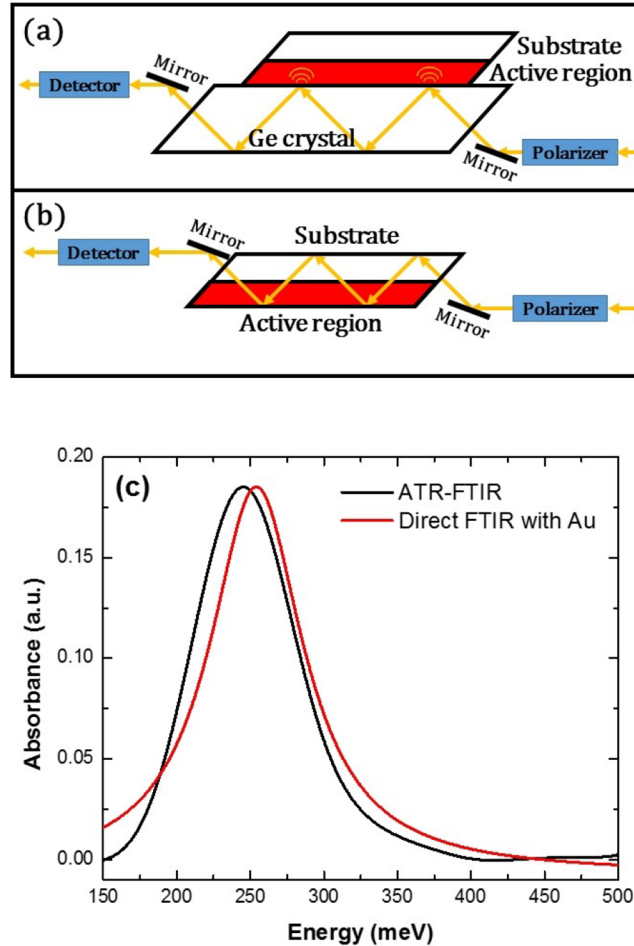


Fig. 3. Experimental setup for (a) ATR-FTIR and (b) direct-FTIR ISBA measurement techniques. (c) ISBA spectra for sample A using direct-FTIR (red curve), and ATR-FTIR (black curve) method. The direct-FTIR absorption was enhanced by depositing a 100 nm Au thin film on top of the MQWs. The ATR-FTIR curve was rescaled to have approximately the same height as the direct-FTIR curve.

We used the Nextnano++ software package to calculate the electronic band structure of single QWs using the 8-band $\mathbf{k}\cdot\mathbf{p}$ model and the structural parameters from HRXRD and HRHAADF-STEM [31]. The program solves the Schrödinger and Poisson equations self-consistently to estimate the electronic energy levels and the amount of activated charge inside each QW using generally accepted nitride material parameters [32]. The results of these Nextnano++ simulations are referred to as bare (or uncorrected) energy in the discussion below. We then correct the ISB transition energies for many-body effects including exchange-correlation, depolarization, and excitonic corrections [33,34]. The exchange-correlation correction was estimated following two different approaches: the Hartree-Fock approximation (HFA) and the local density approximation (LDA) [35–38].

3. Intersubband absorption results

Figure 3(c) shows representative ISBA spectra collected for sample A with both the ATR-FTIR and direct FTIR techniques. Since sample A had only 15 QWs, while the other samples listed in Table 1 have 30 QWs, a 100 nm Au thin film was deposited on top of the MQWs to enhance ISB absorption in the direct measurement by changing the boundary condition for the electric field standing wave from node to anti-node [29]. Since the ATR-FTIR absorption peak depends on the evanescent wave penetration depth that in turn is greatly affected by the air gap between the Ge crystal and the specimen, the ATR-FTIR curve was re-scaled to the same maximum as that of the direct-FTIR curve. The spectra show qualitatively similar ISBA peaks at 246 meV and 254 meV for the ATR-FTIR and direct FTIR measurements, respectively. There is good agreement for the absorption energy from both methods for this sample.

Table 1 summarizes the experimental results of our investigation of ISB absorption for a series of non-polar m-plane (In)AlGa_N/InGa_N MQWs. The ISBA peak energy and full-width at half maximum (FWHM) of both ATR- and direct-FTIR experiments are determined by fitting the measured curves with Lorentzian line shapes. Experimental uncertainty bars for transition energies in subsequent plots of ± 20 meV are due to peak fitting variance. Notice that, consistently throughout all samples, the ISBA energy measured using the ATR-FTIR technique is smaller than the value from the direct-FTIR measurement. This trend may be due to the evanescent wave in the ATR geometry whose penetration depth is proportional to wavelength. The observed red shift of the ATR-FTIR peak compared to the direct-FTIR peak might be caused by enhanced absorbance strength in the ATR spectra at longer wavelength (smaller energy) relative to shorter wavelength (larger energy). Alternatively, the direct FTIR peak position may be affected by background absorption by defects in the free-standing GaN substrate. Since the origin of this energy difference is not clear at this time, we report the results from both experimental techniques.

To understand ISBA in non-polar m-plane (In)AlGa_N/InGa_N MQWs and evaluate its potential for infrared optoelectronics, we examined the theoretical and experimental dependence of transition energies on four critical material parameters: CBO, Al-composition, sheet charge density, and QW width. For clarity, the MQW samples are organized into groups according to the structural parameter that was intentionally varied: Al composition (group I), doping level (group II), and QW thickness (group III). Some samples belong to more than one group. Samples in group I (A, B, and C) contain increasingly higher Al-composition in the barriers. As the Al composition increases, we expected to observe an increase in CBO and ISB absorption energy. Samples in group II (C, D, E, and F) have essentially the same structure, but were doped at different levels. When the sheet charge density is increased, the ISB absorption energy is expected to increase and eventually becomes saturated [9]. Furthermore, the FWHM of the spectrum which is dominated by impurity scattering also increases with the doping level. This explains the unusually large FWHM of the ATR-FTIR spectrum for sample D. Lastly, group III samples (F, G, H, and I) have different QW thicknesses to examine the effect of this parameter on ISBA transition energy.

4. Discussion

The barrier height plays a major role in determining the ISB transition energies of QWs with finite barriers. However, the band offsets for m-plane (In)_yAl_xGa_{1-x-y}N/In_yGa_{1-y}N (with $x < 0.3$ and $z < 0.3$) are not well understood at this point and deserve more experimental investigation in the future. Since considerably more information is available in the literature for the band offsets of c-plane AlGa_N/Ga_N and Ga_N/InGa_N heterostructures [6,11,39–48], we use them as a starting point in our calculations. They provide a CBO of approximately 512 meV for Al_{0.25}Ga_{0.75}N/In_{0.16}Ga_{0.84}N MQWs. Figure 4 shows the effect of CBO variation on the calculated ISB transition energy for QWs with the structure of sample F. The black curve indicates the

variation of the bare transition energy with CBO. The blue and green curves are ISB transition energies corrected using the HFA and LDA, respectively. Uncertainty bands corresponding to experimental QW thickness uncertainty of ± 0.25 nm are also indicated on the figure for these two curves. The flat red curve shows the direct-FTIR measured transition energy for sample F centered within a fitting uncertainty band given by ± 20 meV. While HFA requires a CBO ≤ 475 meV for agreement between experimental and calculated transition energy, LDA suggests $420 \text{ meV} \leq \text{CBO} \leq 600$ meV. The latter range is consistent with our initial estimate based on c-plane AlGaIn/GaN and GaN/InGaIn band offsets. Therefore, we believe that this is the first strong evidence that the LDA is a more suitable approximation for many-body corrections in m-plane nitride heterostructures.

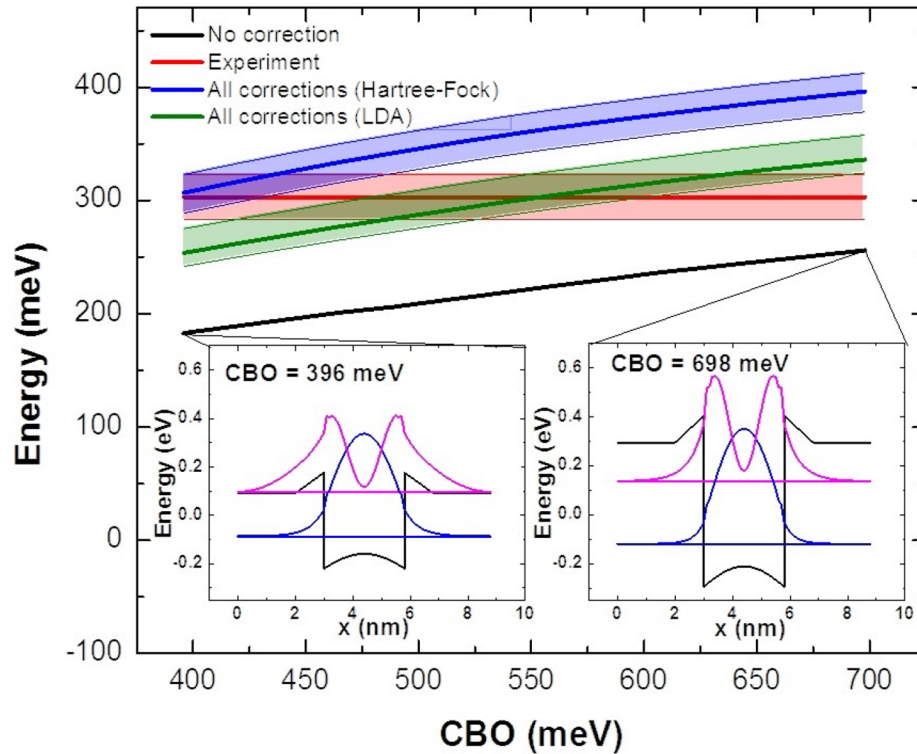


Fig. 4. Effect of CBO on calculated ISB absorption energy with HFA and LDA corrections for a QW with the structure of sample F. The ISB absorption energy measured with direct-FTIR for sample F is also shown for comparison with theoretical calculations. The insets show the conduction band edge and the wavefunctions for the two lowest energy states for CBOs corresponding to the ends of the considered range.

Next, we examine the accuracy of many-body corrections in predicting the dependence of ISB transition energies on charge density. The samples in group II (C-F) have the same nominal structure, but different amounts of charge due to δ -doping at four different levels. Figure 5 compares the many-body effects on ISBA energy as a function of sheet charge density using (a) HFA and (b) LDA for a CBO of 512 meV based on the values accepted in the literature for c-plane nitride heterostructures. The black curve shows the ISBA energy without any correction, while the other curves present the calculated ISBA energies corrected for excitonic, depolarization, exchange-correlation, and all effects in blue, red, magenta, and green, respectively. Figure 5(a) indicates that the HFA significantly overestimates the total corrected energy regardless

of experimental technique. In contrast, Fig. 5(b) adequately reproduces the experimental values for ATR-FTIR, while slightly underestimating the measured direct-FTIR values. The discrepancy between the two calculation methods is due to the exchange-correlation term of the many-body corrections. The overestimation of exchange-correlation correction in HFA has been reported before [29], and has been attributed to omission of some correlation effects. Our experimental results again point out that LDA is more suitable for calculating the exchange-correlation correction for these materials.

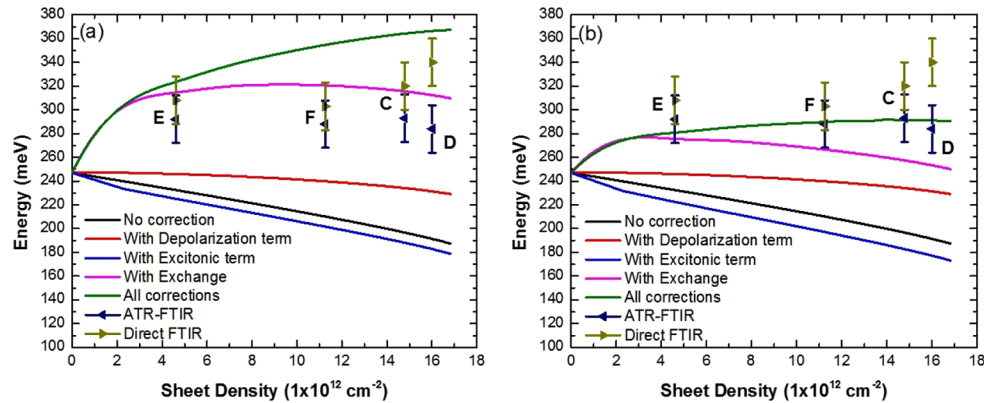


Fig. 5. Effect of charge density on ISBA energy of group II samples and calculated transition energies using a CBO of 512 meV and many-body corrections with (a) HFA and (b) LDA.

The small difference between experimental ISBA energies measured using direct-FTIR and LDA calculations (Fig. 5(b)) may be due to uncertainties in the measurements or to a lower CBO employed in the calculations (512 meV) than that of our (In)AlGaIn/InGaIn samples. We have relatively high confidence in the structural parameters derived from two independent techniques (i.e. HRXRD and HRHAADF-STEM), but acknowledge uncertainties related to direct-FTIR background subtraction (see discussion above). Furthermore, knowledge of CBO for our experimental alloy combinations on m-plane GaN is very limited. It is important to note that there are several reports that suggest much higher CBO for non-polar a-plane AlGaIn/GaN [6,11,39–48] than for c-plane AlGaIn/GaN. These reports attribute the discrepancies between c-plane and a-plane CBOs to uncertainties in correcting for built-in electric fields for c-plane heterostructures. Therefore, it would be straightforward to adjust the CBO to obtain a better quantitative agreement between calculations using LDA and direct-FTIR measurements. A 16% CBO increase would yield excellent agreement between the LDA calculations and the direct-FTIR experimental values. Given the differences between our two spectroscopic data sets, though, we choose to keep the CBO at the value derived from literature for the rest of the discussion.

The third group of samples (H-I) was designed to probe the dependence of ISBA energy and FWHM on QW thickness. Figure 6 compares the ISBA energy dependence on QW width for the samples in group III (H-I) with the theoretical calculations using HFA and LDA. Both experimental data and calculations show the expected decrease of ISB transition energy with increasing QW width. Similar to the results discussed above, the HFA overestimates the ISBA energy, while LDA is in better quantitative agreement with measured values. This observation further substantiates our conclusion that LDA is more accurate in predicting ISBA energies of our nonpolar nitride MQWs than HFA.

Except for sample H, our samples exhibit linewidths (minimum FWHM = 55 meV) comparable to the narrowest reported in the literature for this ISB energy range [19,23]. This is likely due to low impurity scattering and low interface roughness. For the very narrow QWs of sample H (Fig. 1(a)), the band structure calculations indicate that the first excited electronic state is not

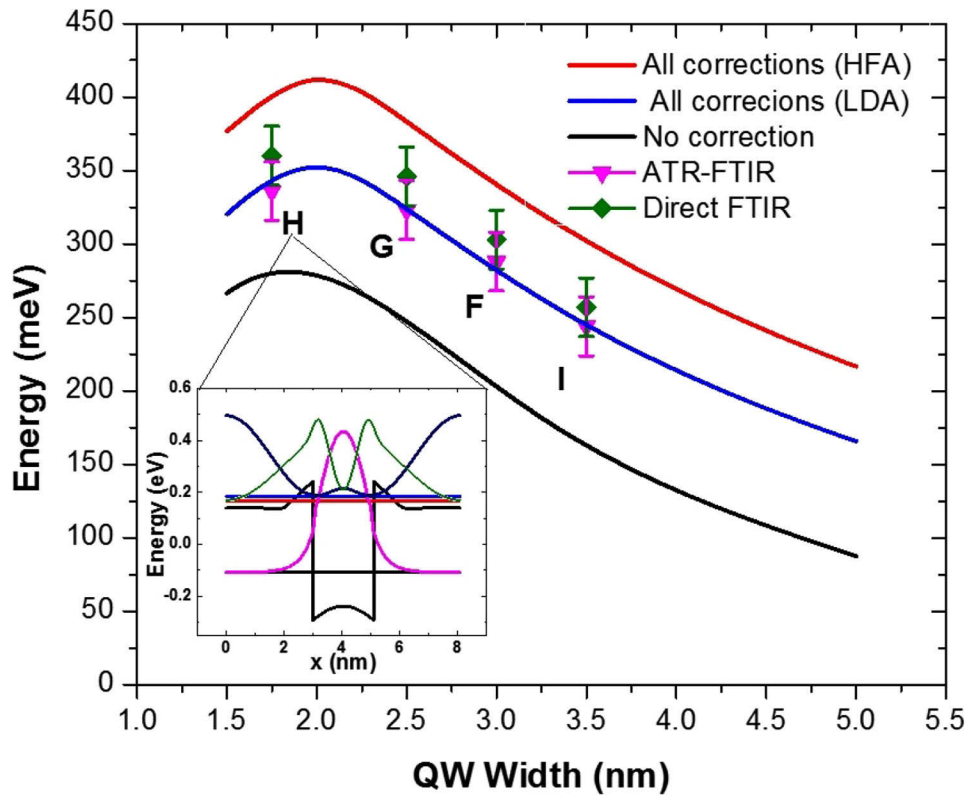


Fig. 6. The effect of QW width on experimental ISBA energy for samples in group III. Calculated transition energies using HFA (red) and LDA (blue) are also shown for comparison. The inset shows the calculated conduction band edge and wavefunctions corresponding to the lowest energy states for sample H. The first QW excited state of sample H is 15 meV below the lowest lying state localized in the barrier.

only located very close to the top of the barrier, but also about 15 meV below the ground state of the electron in the barrier (inset of Fig. 6). Therefore, the crossing of the states localized in the QW and barrier may create a superlattice mini-band that broadens the absorption spectrum and explains the abnormally large FWHM of sample H (324 meV).

Finally, we explore the effect of the Al-composition variation on the ISBA spectrum for a fixed QW width. Specifically, we are interested in identifying the Al fraction that results in near-infrared ISB transitions. This investigation also gives an additional opportunity to test the accuracy of HFA and LDA in non-polar m-plane (In)AlGa_N/InGa_N heterostructures. Figure 7 shows the experimental ISB energies of the samples in group I (A-C) and compares them with theoretical calculations for the layer structure of sample A. The black, blue, and red curves show the calculated energies without any correction, total corrected energies with LDA, and with HFA, respectively. Consistent with the previous discussion, LDA slightly underestimates ISBA energy, while HFA significantly overestimates the transition energies. Neither approach perfectly reproduces the experimental results, but the LDA appears to be more accurate.

The experimentally accessible Al composition in our MBE-grown samples is limited by material defects. STEM images of samples B (Fig. 1(b-d)) reveal alloy inhomogeneity in QBs. With increasing Al composition, Al-rich regions start forming causing non-uniform barrier material and increased interface roughness. This type of inhomogeneity likely has

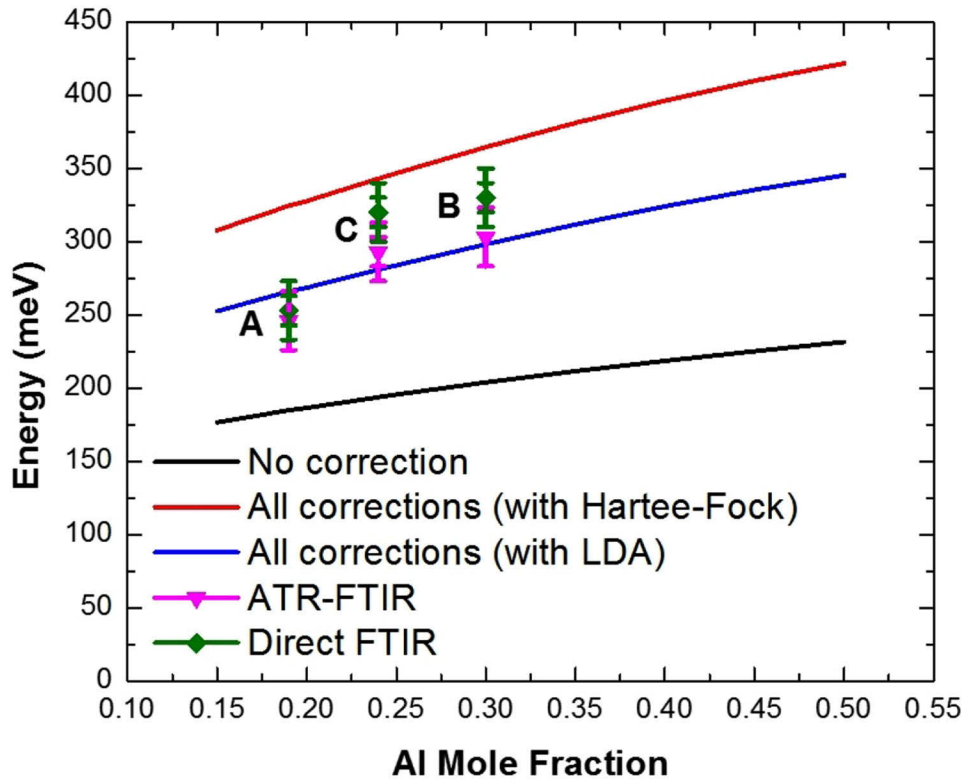


Fig. 7. Effect of aluminum composition on ISB transition energy for the samples in group I (A-C) as compared with theoretical ISBA energies calculated for the layer structure corresponding to sample A using HFA (red) and LDA (blue).

the same cause as the growth instability we reported above 60% Al-composition in non-polar m-plane AlGa_N/Ga_N MQWs [9,10]. Inhomogeneities become visible at considerably lower Al-composition (i.e. Al_{0.3}Ga_{0.7}N) in this study, though, due to the lower growth temperature necessary for incorporating indium in the QWs (565°C) compared to our previous study [10].

The theoretical calculations shown in Fig. 7 allow us to probe the Al composition necessary for AlGa_N/In_{0.16}Ga_{0.84}N MQWs to absorb in the near-infrared regime (below 3 μm). Figure 7 suggests that even though the HFA predicts near-IR transition energies for QB composition below 50%, potentially more accurate LDA calculations indicate that this range is not accessible with the available indium composition in the QW. Given the composition limitations imposed by defects in AlGa_N, we can conclude that further increasing the ISB transition energy in m-plane AlGa_N/InGa_N MQWs can only be achieved by further increasing the indium composition in the QWs.

5. Conclusion

This paper reports for the first time ISBA in strain-balanced non-polar m-plane (In)AlGa_N/InGa_N MQWs grown by plasma-assisted MBE. Direct- and ATR-FTIR measurements are in agreement with each other, but the ATR-FTIR technique consistently produces lower transition energies. The measured ISB transitions span the range 3.4 to 5.1 μm and exhibit linewidths comparable with the narrowest linewidths reported in the literature for m-plane AlGa_N/Ga_N MQWs. Calculations of

the ISB transition energies revealed that they are extremely sensitive to the choice of conduction-band offset. If we assume the CBO derived from band offsets measured for c-plane nitride alloys, then the LDA is more suitable for reproducing experimental transition values than the HFA. Overall, LDA slightly underestimates the ISB energies, but the remaining discrepancy with experimental values may be compensated by a moderate increase of the CBO. The ISBA energies exhibit the expected dependence on charge density, QW width, and barrier Al composition. However, the energies fall short of reaching the technologically relevant near-infrared range. More research is needed to further increase the CBO primarily by increasing the In-composition in the QWs.

Funding. US National Science Foundation (ECCS-1607173); Directorate for Mathematical and Physical Sciences (DMR-1610893, DMR-2004462).

Acknowledgements. We acknowledge support from the National Science Foundation. TN, YC, and OM were supported in part by NSF awards DMR-1610893, and DMR-2004462. BD and AS acknowledge partial support from NSF award ECCS-1607173. All STEM imaging and analyses were performed at the Electron Microscopy Facility at Birck Nanotechnology Center, Purdue University.

Disclosures. The authors declare no conflicts of interest.

Data availability. Data underlying the results presented in this paper are not publicly available at this time but may be obtained from the authors upon reasonable request.

References

1. S. Nakamura, M. Senoh, N. Iwasa, and S.-I. Nagahama, "High-brightness InGa_N blue, green and yellow light emitting diodes with quantum well structures," *Jpn. J. Appl. Phys.* **34**(2), L797–L799 (1995).
2. S. Nakamura, "InGa_N/AlGa_N blue-light-emitting diodes," *J. Vac. Sci. Tech. A* **13**(3), 705–710 (1995).
3. S. Nakamura, T. Mukai, and M. Senoh, "High-brightness InGa_N/AlGa_N double-heterostructure blue-green-light-emitting diodes," *J. Appl. Phys.* **76**(12), 8189–8191 (1994).
4. S. Nakamura, "Growth of In_xGa_(1-x)N compound semiconductors and high-power InGa_N/AlGa_N double heterostructure violet-light-emitting diodes," *Microelectronics J.* **25**(8), 651–659 (1994).
5. S. Nakamura, T. Mukai, and M. Senoh, "Candela-class high-brightness InGa_N/AlGa_N double-heterostructure blue-light-emitting diodes," *Appl. Phys. Lett.* **64**(13), 1687–1689 (1994).
6. D. Feezell and S. Nakamura, "Invention, development, and status of the blue light-emitting diode, the enabler of solid state lighting," *C. R. Phys.* **19**(3), 113–133 (2018).
7. M. Beeler, E. Trichas, and E. Monroy, "III-nitride semiconductors for intersubband optoelectronics: a review," *Semicond. Sci. Technol.* **28**(7), 074022 (2013).
8. J. Wu, "When group-III nitrides go infrared: New properties and perspectives," *J. Appl. Phys.* **106**(1), 011101 (2009).
9. T. Nguyen, M. Shirazi-HD, Y. Cao, R. E. Diaz, G. C. Gardner, M. J. Manfra, and O. Malis, "Intersubband transition in nonpolar m-plane AlGa_N/Ga_N heterostructures," *Phys. Status Solidi A* **215**(13), 1700828 (2018).
10. M. Shirazi-HD, R. E. Diaz, T. Nguyen, J. Jian, G. C. Gardner, H. Wang, M. J. Manfra, and O. Malis, "Kinetic instability of AlGa_N alloys during MBE growth under metal-rich conditions on m-plane Ga_N miscut towards the $-c$ axis," *J. Appl. Phys.* **123**(16), 161581 (2018).
11. A. Pesach, E. Gross, C.-Y. Huang, Y.-D. Lin, S. E. Schacham, S. Nakamura, and G. Bahir, "Non-polar m-plane intersubband based InGa_N/(Al)Ga_N quantum well infrared photodetectors," *Appl. Phys. Lett.* **103**(2), 022110 (2013).
12. J. S. Speck and S. F. Chichibu, "Nonpolar and semipolar group III nitride-based materials," *MRS Bull.* **34**(5), 304–312 (2009).
13. A. Ajay and E. Monroy, "Intersubband transitions in Ga_N-based heterostructures," *Mid-infrared Optoelectronics*, 539–565 (2020).
14. C. B. Lim, M. Beeler, A. Jay, J. Lahmann, E. Bellet-Amalric, C. Bougerol, and E. Monroy, "Intersubband transitions in nonpolar Ga_N/Al(Ga)_N heterostructures in the short- and mid-wavelength infrared regions," *J. Appl. Phys.* **118**(1), 014309 (2015).
15. G. Chen, X. Q. Wang, X. Rong, P. Wang, F. J. Xu, N. Tang, Z. X. Qin, Y. H. Chen, and B. Shen, "Intersubband transition in Ga_N/InGa_N multiple quantum wells," *Sci. Rep.* **5**(1), 11485 (2015).
16. M. Li, Y. W. Lu, D. B. Li, X. X. Han, Q. S. Zhu, X. L. Liu, and Z. G. Wang, "Effect of spontaneous and piezoelectric polarization on intersubband transition in Al_xGa_{1-x}N-Ga_N quantum well," *J. Vac. Sci. Technol., B* **22**(6), 2568 (2004).
17. K. Kishino, A. Kikuchi, H. Kanazawa, and T. Tachibana, "Intersubband transition in (Ga_N)_m/(Al_N)_n superlattices in the wavelength range from 1.08 to 1.61 μm ," *Appl. Phys. Lett.* **81**(7), 1234–1236 (2002).
18. D. Feezell, Y. Sharma, and S. Krishna, "Optical properties of nonpolar III-nitrides for intersubband photodetectors," *J. Appl. Phys.* **113**(13), 133103 (2013).
19. T. Kotani, M. Arita, and Y. Arakawa, "Observation of mid-infrared intersubband absorption in non-polar m-plane AlGa_N/Ga_N multiple quantum wells," *Appl. Phys. Lett.* **105**(26), 261108 (2014).

20. T. Kotani, M. Arita, and Y. Arakawa, "Doping dependent blue shift and linewidth broadening of intersubband absorption in non-polar m-plane AlGaIn/GaN multiple quantum wells," *Appl. Phys. Lett.* **107**(11), 112107 (2015).
21. C. Edmunds, L. Tang, D. Li, M. Cervantes, G. Gardner, T. Paskova, M. J. Manfra, and O. Malis, "Near-infrared absorption in lattice-matched AlInN/GaN and strained AlGaIn/GaN heterostructures grown by MBE on low-defect GaN substrates," *J Electron. Matter.* **41**(5), 881–886 (2012).
22. C. Edmunds, J. Shao, M. Shirazi-HD, M. J. Manfra, and O. Malis, "Terahertz intersubband absorption in non-polar m-plane AlGaIn/GaN quantum wells," *Appl. Phys. Lett.* **105**(2), 021109 (2014).
23. M. Monavarian, J. Xu, M. N. Fireman, N. Nookala, F. Wu, B. Bonef, K. S. Qwah, E. C. Young, M. A. Belkin, and J. S. Speck, "Narrow linewidth characteristics of interband cascade lasers," *Appl. Phys. Lett.* **116**(20), 201103 (2020).
24. J. Shao, D. Zakharov, C. Edmunds, O. Malis, and M. J. Manfra, "Homogeneous AlGaIn/GaN superlattices grown on free-standing (1-100) GaN substrates by plasma-assisted molecular beam epitaxy," *Appl. Phys. Lett.* **103**(23), 232103 (2013).
25. J. Shao, L. Tang, C. Edmunds, G. Gardner, O. Malis, and M. J. Manfra, "Surface morphology evolution of m-plane (1-100) GaN during molecular beam epitaxy growth: Impact of Ga/N ratio, miscut direction, and growth temperature," *J. Appl. Phys.* **114**(2), 023508 (2013).
26. M. N. Fireman, B. Bonef, E. C. Young, N. Nookala, M. A. Belkin, and J. S. Speck, "Strain compensated superlattices on m-plane gallium nitride by ammonia molecular beam epitaxy," *J. Appl. Phys.* **122**(7), 075105 (2017).
27. A. Senichev, B. Dzuba, T. Nguyen, Y. Cao, M. A. Capano, M. J. Manfra, and O. Malis, "Impact of growth conditions and stain on indium incorporation in non-polar m-plane (10-10) InGaIn grown by plasma-assisted molecular beam epitaxy," *APL Material* **7**(12), 121109 (2019).
28. B. Dzuba, A. Senichev, T. Nguyen, Y. Cao, R. E. Diaz, M. J. Manfra, and O. Malis, "Indium surfactant assisted epitaxy of non-polar (10-10) AlGaIn/InGaIn multiple quantum well heterostructures," *J. Appl. Phys.* **128**(11), 115701 (2020).
29. M. Helm, "The basic physics of intersubband transition," in *Intersubband Transition in Quantum Wells: Physics and Device Applications I* (Elsevier, 1999), Vol. 62, pp. 1–99.
30. C. Edmunds, L. Tang, J. Shao, D. Li, M. Cervantes, G. Gardner, D. N. Zakharov, M. J. Manfra, and O. Malis, "Improvement of near-infrared absorption linewidth in AlGaIn/GaN superlattices by optimization of delta-doping location," *Appl. Phys. Lett.* **101**(10), 102104 (2012).
31. S. Birner, T. Zibold, T. Andlauer, T. Kubis, M. Sabathil, A. Trellakis, and P. Vogl, "Nextnano: general purpose 3-D simulations," *IEEE Trans. Electron. Devices* **54**(9), 2137–2142 (2007).
32. I. Vurgaftman and J. R. Meyer, "Band parameters for nitrogen-containing semiconductors," *J. Appl. Phys.* **94**(6), 3675–3696 (2003).
33. T. Ando, "Density-functional calculation of subband structure on semiconductor surfaces," *Surf. Sci.* **58**(1), 128–134 (1976).
34. S. J. Allen Jr, D. C. Tsui, and B. Vinter, "On the absorption of infrared radiation by electrons in semiconductor inversion layers," *Solid State Communication* **20**(4), 425–428 (1976).
35. K. M. Bandara, D. D. Coon, O. Byungsung, Y. F. Lin, and M. H. Francombe, "Exchange interaction in quantum well subbands," *Appl. Phys. Lett.* **53**(20), 1931–1933 (1988).
36. W. L. Bloss, "Effects of Hartree, exchange, and correlation energy on intersubband transitions," *J. Appl. Phys.* **66**(8), 3639–3642 (1989).
37. L. Helden and B. I. Lundqvist, *J. Phys. C: Solid St. Phys.* **4**, 2064 (1971).
38. K. M. Bandara, D. D. Coon, O. Byungsung, Y. F. Lin, and M. H. Francombe, "Erratum: Exchange interactions in quantum wells subbands," *Appl. Phys. Lett.* **55**(2), 206 (1989).
39. R. Basanta, K. Mahesh, R. K. Mohana, B. N. Thirumaleshwara, and S. B. Krupanidhi, "Dynamics of the spatial electron density distribution of EUV-induced plasmas," *J. Phys. D: Appl. Phys.* **48**(43), 432001 (2015).
40. U. Hilmi and A. Asen, "Band offsets in III-nitride heterostructures," *J. Phys. D: Appl. Phys.* **35**(7), 591–594 (2002).
41. Y. Tsai and C. Bayram, "Band alignments of ternary wurtzite and zincblende III-nitrides investigated by hybrid density functional theory," *ACS Omega* **5**(8), 3917–3923 (2020).
42. Y. Gao, D. Sun, X. Jiang, and J. Zhao, "Ab initio analytic calculation of point defects in AlGaIn/GaN heterointerfaces," *J. Phys.: Condens. Matter* **33**(3), 035002 (2021).
43. S. Wei and A. Zunger, "Valence band splittings and band offsets of AlN, GaN, and InN," *Appl. Phys. Lett.* **69**(18), 2719–2721 (1996).
44. A. N. Westmeyer, S. Mahajan, K. K. Bajai, J. Y. Lin, H. X. Jiang, D. D. Kileske, and R. T. Senger, "Determination of energy-band offsets between GaN and AlN using excitonic luminescence transition in AlGaIn alloys," *J. Appl. Phys.* **99**(1), 013705 (2006).
45. K. A. Wang, C. Lian, N. Su, and D. Jena, "Conduction band offset at the InN/GaN heterojunction," *Appl. Phys. Lett.* **91**(23), 232117 (2007).
46. A. Hurni, H. Kroemer, U. K. Mishra, and J. S. Speck, "m-plane (10-10) and (20-21) GaN/Al_xGa_{1-x}N conduction band offsets measured by capacitance-voltage profiling," *Appl. Phys. Lett.* **105**(23), 232108 (2014).
47. L. Sang, Q. S. Zhu, S. Y. Yang, G. P. Liu, H. J. Li, H. Y. Wei, C. M. Jiao, S. M. Liu, Z. G. Wang, X. W. Zhou, W. Mao, Y. Hao, and B. Shen, "Band offsets of non-polar A-plane GaN/AlN and AlN/GaN heterostructures measured by X-ray photoemission spectroscopy," *Nanoscale Res Lett* **9**(1), 470 (2014).

48. P. Reddy, I. Bryan, Z. Bryan, J. Tweedie, S. Washiyama, R. Kirste, S. Mita, R. Collazo, and Z. Sitar, "Charge neutrality levels, barrier heights, and band offsets at polar AlGa_N," *Appl. Phys. Lett.* **107**(9), 091603 (2015).